IEEE Journal of Emerging and Selected Topics in Power Electronics, pp. 1–1, 2020

Hardware-in-the-Loop Characterization of Source-Affected Output Characteristics of Cascaded H-Bridge Converter

M. Petković and D. Dujić

POWER ELECTRONICS LABORATORY
ÉCOLE POLYTECHNIQUE FÉDÉRALE DE LAUSANNE

This article has been accepted for publication in a future issue of this journal, but has not been fully edited. Content may change prior to final publication. Citation information: DOI 10.1109/JESTPE.2020.2994369, IEEE Journal of Emerging and Selected Topics in Power Electronics

Hardware-in-the-Loop Characterization of Source-Affected Output Characteristics of Cascaded H-Bridge Converter

Marko Petković, *Student Member, IEEE,* Dražen Dujić, *Senior Member, IEEE*
Power Electronics Laboratory, École Polytechnique Fédérale de Lausanne
marko.petkovic@epfl.ch; drazen.dujic@epfl.ch

***Abstract*—Recent trends in power system design such as an increasing share of renewable energy sources and integration of power electronics equipment for medium voltage applications are creating different subsystem interactions that require proper investigation, understanding, description, and estimation of global system stability through impedance-admittance measurements and identification. Four-quadrant Cascaded H-Bridge topology features high output voltage resolution and high effective switching frequency which enables high-dynamic, high-fidelity voltage perturbation injection for medium voltage impedance measurement. This paper assesses the impact that the active element on the input side has on the output side, where the injection of the perturbation signal is realized. Models of the input and output element are developed as well as the model of the connected system. To validate the theoretical developments, a new method to measure the single-phase output dynamics in the *dq*-frame is proposed and the measurement is performed using offline and real-time simulations on a hardware-in-the-loop platform.**

***Index Terms*—dq-frame, measurement, modelling, single-phase, source-affected,**

I. Introduction

The rapid increase in energy demand in combination with advances in the field of power electronics has led to the deployment of renewable energy systems as well as broader installation of power conversion devices. This trend has subsequently led to a change in power network behaviour that is becoming increasingly complex. Due to the complexity of the installations, it becomes more challenging to model the system and predict possible instabilities that arise as a result of the interaction of different elements in the grid [1], [2]. Early identification and characterization of the present system and its future potential components would reduce the risk of encountering unpredictable behavior which would, in turn, provide a stable network with uninterrupted operation. Some of the criteria used to assess the stability are presented in [3] and they rely either on analysing the minor-loop gain or the passivity of the system. Whatever the criteria are, the knowledge of the impedance of the network being analysed is required.

The topic of low voltage (LV) impedance / admittance measurement has already been treated in different publications. The authors of [4] have presented an overview of different measurement techniques based in the frequency domain, with different proposals on the practical implementations of perturbation injection converters (PICs) whereas the measurements based on wideband signal injection were presented in [5], [6]. In general, impedance measurement in low-power and LV ranges for the design of power supplies is a mature and well-established technology. Devices capable of operating at $1\,\mathrm{kV}$ and up to power rating of $200\,\mathrm{kVA}$ are present in the form of grid emulators, which are well suited for perturbing systems as they are capable of outputting an external waveform reference.

On the other hand, the problem of high-power and medium voltage (MV) impedance/admittance measurement and system identification had not yet been fully resolved. Such measurements in MV applications are not straightforward as there is a need for a device capable of operating at an MV level and injecting a perturbation into an MV system. At the same time having wide measurement bandwidth is sought after which is not easily achieved at MV level. The research performed in this field is scarce and the devices developed for that purpose are few. Medium voltage impedance / admittance estimators that exist today have been presented in [7]–[10]. These solutions have either limited bandwidth, up to $1\,\mathrm{kHz}$ or feature an output side transformer in order to step-up the voltage to the MV levels. This in turn also limits the bandwidth. Still, the demand for such equipment is growing due to the need to support the development of recent medium voltage dc (MVdc) and medium voltage ac (MVac) applications, grid integration of renewable energy sources and storage devices, energy transmission and distribution in the MV range [11]–[13] and assure safe integration with the existing apparatus.

One of the topologies capable of having sufficiently high voltage output and bandwidth is based on Cascaded H-Bridge (CHB) with an active input element interfaced to a multi-winding transformer (MWT), which was already presented in [14], where the feasibility of using a multilevel topology for perturbation injection was studied. The topology consists of step-down MV–MWT with 15 secondary phase-shifted outputs permitting to stack up to 5 cells per phase and thus effectively increase the output voltage levels and switching frequency allowing higher frequency voltage perturbation injection and impedance measurement. As a matter of fact, the presence of the MWT on the input side is one of the advantages of this topology. Having the MWT at the input means that there is no need to have a step-up transformer on the output side to elevate the voltage to MV level. As a result, the output stage high-frequency bandwidth is not limited by the output transformer.

This article has been accepted for publication in a future issue of this journal, but has not been fully edited. Content may change prior to final publication. Citation information: DOI 10.1109/JESTPE.2020.2994369, IEEE Journal of Emerging and Selected Topics in Power Electronics

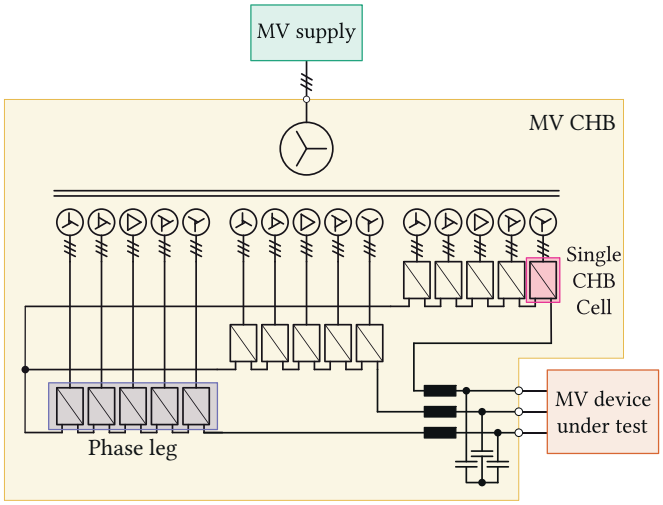

Fig. 1. Cascaded H-bridge topology for high dynamic medium-voltage perturbation injection and impedance measurement.

The CHB cells outputs are interfaced to a three-phase LC-type filter on which the voltage output is controlled. A single cell of the CHB converter is presented in Fig. 2. It consists of an Active Front End (AFE) as the input conversion stage and an H-bridge (HB) inverter as the output conversion stage. It is taken as an assumption that the dynamics of a single-phase leg consisting of five cells can be represented by the dynamics of one cell, which is why the cell in Fig. 2 is represented with an LC-type filter at the output.

The initial study on the feasibility of this solution was performed in [14], where there was a need to superimpose a high-frequency small-signal in addition to the fundamental component. When this is performed in a closed-loop, there exist possible interactions of synchronization and closed control loops of AFE and HB. Our work seeks to reveal if the presence of an active input element, such as AFE, impacts the dynamics of the output element, the HB and subsequently the cascaded connection of multiple HBs.

The motivation for this is that for precise injection of perturbation signal into the device under test (DUT), one needs to ensure that the input side of the CHB does not in any way limit the output and that there are no other frequency components present that may impact the measurements. The methodology to respond to this question puts to use the state-space modelling and presents the model of the cell in the *dq*-frame. To confirm the model there needs to exist a method to measure the single-phase characteristics and represent them in *dq*-frame, which is also covered in this work.

Main novelty of the paper is:

1) Investigation of source-load interactions between the three-phase AFE and single-phase HB in the context of a MV-CHB converter.
2) Modelling of a single-phase HB inverter in the *dq*-frame reinforced by modelling the quadrature signal generator (QSG) in the *dq*-frame, as well.
3) Use of wideband PRBS signal for perturbation injection and measurements. So far, in the context of single-phase *dq*-frame measurements, to the knowledge of authors, only the single-tone signals have been used.
4) Investigation of feasibility of a MV-CHB converter employed as a perturbation injection device for medium-voltage impedance/admittance measurement.

The rest of the paper is organised as follows. Section II describes the main features of a single cell of the CHB converter. Section III provides the state-space model of the cell in the *dq*-frame. Section IV characterizes the source-affected dynamics of the cell output. Section V proposed a new method for measuring control-to-output characteristics in *dq*-frame that makes use of single-phase measurements together with a wideband pseudo-random binary sequence (PRBS) signal. Section VI presents results and a practical application of measuring an input impedance of a MV grid-connected converter. Finally, Section VII concludes the work.

II. Cascaded H-Bridge Cell

The MWT (c.f. Fig. 1) supplies three-phase isolated voltages from its secondary, low-voltage side to the cell. Isolated three-phase supply makes the cells and the dc-links largely independent from each other [15]. The input filter of the cell is the L-type filter with its parasitic resistance, which can be realized as a discrete inductor or through leakage inductance of the MWT [16]. The rectification of the input voltage is performed by the three-phase AFE switching at $f_{\mathrm{sw}}^{\mathrm{AFE}} = 10\,\mathrm{kHz}$. The supply voltage is rectified to $1.2\,\mathrm{kV}$ at the dc-link. The dc-link serves as an energy buffer from which the output stage, a single-phase HB, switching at $f_{\mathrm{sw}}^{\mathrm{HB}} = 20\,\mathrm{kHz}$ is supposed to inject perturbation voltages, through an LC-type filter into an unknown network or DUT. The output stage is a SiC based one, thus enabling such high switching frequency. The AFE control system comprises a PLL that performs synchronisation, as it is essentially a grid-connected converter through the MWT [16]. Apart from this, it also performs the cascaded control of the dc-link voltage through the input current control. On the output side, the HB performs cascaded control of its output voltage through the control of the filter inductor current.

Ideally, for the best possible impedance identification of the DUT, the output stage should be completely decoupled from the input one and the presence of the active element with its control should not be a limiting factor for impedance measurement.

III. Single Cell Modelling

A. Active Front End Modelling

Closed-loop modelling of the AFE follows the state-space modelling approach outlined in [17], [18] and the intermediate developments are not given in this work, but only the final open-loop and closed-loop models in the Synchronous Reference Frame (SRF) are presented. State-variables of the model are the input current i_g and output voltage v_{dc}, which are also the output variables. Input variables are the supply voltage v_g, load current on the dc side i_{dc} and the duty cycle d^{AFE}. State-space averaged model is presented in Eq. (1), where V_{dc}, D_d^{AFE}, D_q^{AFE}, I_{gd} and I_{gq} are steady-state values of dc-link

This article has been accepted for publication in a future issue of this journal, but has not been fully edited. Content may change prior to final publication. Citation information: DOI 10.1109/JESTPE.2020.2994369, IEEE Journal of Emerging and Selected Topics in Power Electronics

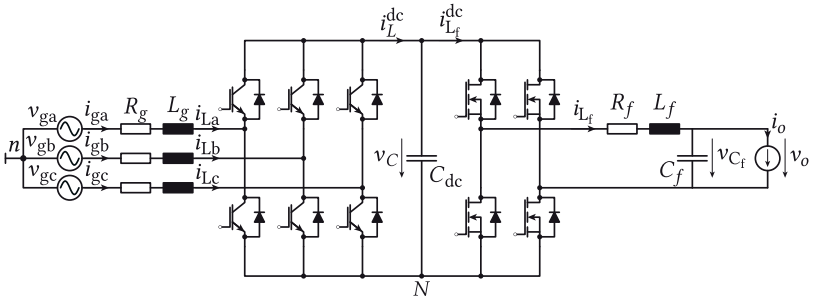

Fig. 2. Three-phase supplied Active Front End (AFE) interfaced to single phase inverter with an LC filter.

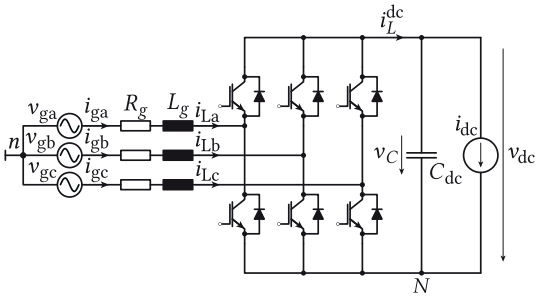

Fig. 3. Ideal three-phase AFE feeding a dc load, CHB in reality, and being supplied from the secondaries of the MWT.

TABLE I: Model parameters

$P_{\mathrm{in}} = 36\,\mathrm{kW}$	$v_{\mathrm{dc}} = 1.2\,\mathrm{kV}$
$v_{\mathrm{g,d}} = 580\,\mathrm{V}$	$f_g = 50\,\mathrm{Hz}$
$v_{\mathrm{g,q}} = 0\,\mathrm{V}$	$L_g = 5.4\,\mathrm{mH}$
$i_{\mathrm{g,d}} = 41.5\,\mathrm{A}$	$R_g = 10\,\mathrm{m\Omega}$
$i_{\mathrm{g,q}} = 0\,\mathrm{A}$	$C_{\mathrm{dc}} = 5\,\mathrm{mF}$
$K_{\mathrm{p,gcc}} = 18$	$K_{\mathrm{i,gcc}} = 33$
$K_{\mathrm{p,dvc}} = 1.4$	$K_{\mathrm{i,dvc}} = 192$

voltage with duty cycles and currents represented in *dq*-frame. To obtain the open-loop dynamics the model in Eq. (1) can be solved using

$$\mathbf{G} = \mathbf{C}(s\mathbf{I} - \mathbf{A})^{-1}\mathbf{B} + \mathbf{D} \tag{2}$$

The open-loop dynamics is represented using

$$\begin{bmatrix} \tilde{\mathbf{i}}_{\mathrm{g,dq}} \\ \tilde{v}_{\mathrm{dc}} \end{bmatrix} = \begin{bmatrix} \mathbf{Y}_{\mathrm{in,o}} & \mathbf{G}_{\mathrm{io,o}} & \mathbf{G}_{\mathrm{ci,o}} \\ \mathbf{T}_{\mathrm{oi,o}} & -Z_{\mathrm{out,o}} & \mathbf{G}_{\mathrm{co,o}} \end{bmatrix} \begin{bmatrix} \tilde{\mathbf{v}}_{\mathrm{g,dq}} \\ \tilde{i}_{\mathrm{dc}} \\ \tilde{\mathbf{d}}_{\mathrm{dq}} \end{bmatrix} \tag{3}$$

The direct link between the AFE and HB is the output impedance of the AFE and thus is the element that could influence the dynamics of the HB. For this reason, the next important step is to find the closed-loop output impedance of the AFE. The closed-loop the AFE is controlled in cascaded manner, with the inner loop being the input current control using proportional integral (PI) controllers in the SRF and the outer controller being the dc-link voltage PI controller [19]. Under the current control loop closed, the output impedance is given as

$$Z_{\mathrm{out,cl}}^{\mathrm{gcc}} = -Z_{\mathrm{out,o}} + \mathbf{G}_{\mathrm{co,o}}\left(\mathbf{G}_{\mathrm{dec}} - \mathbf{G}_{\mathrm{PI}}^{\mathrm{i}}\right)\mathbf{H}_{\mathrm{i}}\mathbf{G}_{\mathrm{io,cl}}^{\mathrm{gcc}} \tag{4}$$

where

$$\mathbf{G}_{\mathrm{io,cl}}^{\mathrm{gcc}} = \left[\mathbf{I} - \mathbf{G}_{\mathrm{ci,o}}\left(\mathbf{G}_{\mathrm{PI}}^{\mathrm{i}} - \mathbf{G}_{\mathrm{dec}}\right)\mathbf{H}_{\mathrm{i}}\right]^{-1}\mathbf{G}_{\mathrm{io,o}} \tag{5}$$

Under the dc-link voltage control closed the output impedance is given as

$$Z_{\mathrm{out,cl}}^{\mathrm{dvc}} = -\left(\mathbf{I} + \mathbf{G}_{\mathrm{co,cl}}^{\mathrm{gcc}}\mathbf{G}_{\mathrm{PI}}^{\mathrm{v}}\mathbf{H}_{\mathrm{v}}\right)^{-1} Z_{\mathrm{out,cl}}^{\mathrm{gcc}} \tag{6}$$

where $\mathbf{G}_{\mathrm{dec}}$, $\mathbf{G}_{\mathrm{PI}}^{\mathrm{i}}$ and $\mathbf{G}_{\mathrm{PI}}^{\mathrm{v}}$ are the current controller decoupling matrix, current controller PI regulator and voltage controller PI regulator, respectively, while matrices $\mathbf{H}$ are current and voltage transducer matrices, all given in the Appendix. Parameters given in Table I represent the steady-state voltages and currents in *dq*-frame, dc-link voltage, nominal input, and switching frequencies, input filter values and controller gains. The controller gains were tuned using Magnitude and Symmetrical optimum. For this application this tuning method suffices, but since the control implemented is a cascaded PI control more sophisticated methods can also be used [20]. The AFE with these parameters was simulated in PLECS and its analytical output impedance from Eq. (6) was compared to the impedance obtained from the frequency response. The result is presented in Fig. 4 and it shows a good match. Several things can be noted in the impedance shape. The impedance magnitude has a low value in the low-frequency range due to a high gain of the controller in the same region. The breaking point at $35\,\mathrm{Hz}$ where the impedance has almost unity gain is the closed-loop dc-link control bandwidth. The dip in the characteristics around $100\,\mathrm{Hz}$ is due to the presence of the $100\,\mathrm{Hz}$ notch filter used to filter out dc-link voltage measurement in the case where the HB would be connected on the output side of the AFE, thus single-phase power variation at double frequency would appear. After this point the impedance magnitude falls at a rate $-20\,\mathrm{dB/dec}$ which is caused by the dc-link capacitor influence.

B. Single-Phase HB Inverter Modelling

The single-phase inverter is required to inject perturbations into a DUT, which is why its output voltage control needs to be independent of the input rectification stage. To this end, the focus of this section will be the modelling of the single-phase inverter closed-loop control-to-output transfer function.

This article has been accepted for publication in a future issue of this journal, but has not been fully edited. Content may change prior to final publication. Citation information: DOI 10.1109/JESTPE.2020.2994369, IEEE Journal of Emerging and Selected Topics in Power Electronics

$$s\begin{bmatrix}\tilde{i}_{\mathrm{gd}}\\ \tilde{i}_{\mathrm{gq}}\\ \tilde{v}_{\mathrm{dc}}\end{bmatrix}=\underbrace{\begin{bmatrix}-\frac{R_g}{L_g} & \omega_g & -\frac{D_d^{\mathrm{AFE}}}{L_g}\\ -\omega_g & -\frac{R_g}{L_g} & -\frac{D_q^{\mathrm{AFE}}}{L_g}\\ \frac{3}{2}\frac{D_d^{\mathrm{AFE}}}{C_{\mathrm{dc}}} & \frac{3}{2}\frac{D_q^{\mathrm{AFE}}}{C} & 0\end{bmatrix}}_{\mathbf{A}}\begin{bmatrix}\tilde{i}_{\mathrm{gd}}\\ \tilde{i}_{\mathrm{gq}}\\ \tilde{v}_{\mathrm{dc}}\end{bmatrix}+\underbrace{\begin{bmatrix}\frac{1}{L_g} & 0 & 0 & -\frac{V_{\mathrm{dc}}}{L_g} & 0\\ 0 & \frac{1}{L_g} & 0 & 0 & -\frac{V_{\mathrm{dc}}}{L_g}\\ 0 & 0 & -\frac{1}{C_{\mathrm{dc}}} & \frac{3}{2}\frac{I_{\mathrm{gd}}}{C} & \frac{3}{2}\frac{I_{\mathrm{gq}}}{C}\end{bmatrix}}_{\mathbf{B}}\begin{bmatrix}\tilde{v}_{\mathrm{gd}}\\ \tilde{v}_{\mathrm{gq}}\\ \tilde{i}_{\mathrm{dc}}\\ \tilde{d}_d^{\mathrm{AFE}}\\ \tilde{d}_q^{\mathrm{AFE}}\end{bmatrix}$$

$$\begin{bmatrix}\tilde{i}_{\mathrm{gd}}\\ \tilde{i}_{\mathrm{gq}}\\ \tilde{v}_{\mathrm{dc}}\end{bmatrix}=\underbrace{\begin{bmatrix}1 & 0 & 0\\ 0 & 1 & 0\\ 0 & 0 & 1\end{bmatrix}}_{\mathbf{C}}\begin{bmatrix}\tilde{i}_{\mathrm{gd}}\\ \tilde{i}_{\mathrm{gq}}\\ \tilde{v}_{\mathrm{dc}}\end{bmatrix}+\underbrace{\begin{bmatrix}0 & 0 & 0 & 0 & 0\\ 0 & 0 & 0 & 0 & 0\\ 0 & 0 & 0 & 0 & 0\end{bmatrix}}_{\mathbf{D}}\begin{bmatrix}\tilde{v}_{\mathrm{gd}}\\ \tilde{v}_{\mathrm{gq}}\\ \tilde{i}_{\mathrm{dc}}\\ \tilde{d}_d^{\mathrm{AFE}}\\ \tilde{d}_q^{\mathrm{AFE}}\end{bmatrix} \tag{1}$$

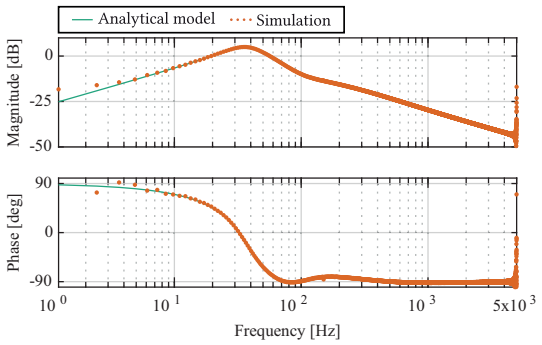

Fig. 4. Output, dc side, impedance of the AFE under the input current and output voltage control loops closed.

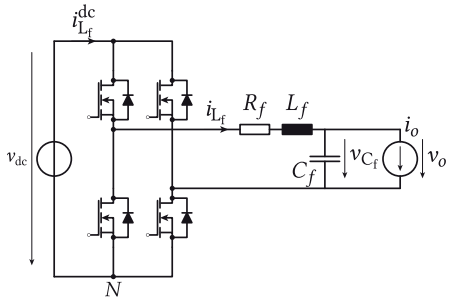

Fig. 5. HB with an output LC filter.

In order to find the closed-loop model, first, the open-loop model and dynamics have to be defined and solved. As the dc-link voltage control is performed on the AFE side, the inverter input is initially treated as an ideal voltage source (c.f. Fig. 5). The inverter output is stage is an LC-type filter and the load is considered to be an ideal current source (or sink). Even though the output stage is a single-phase one, the modelling is performed in the *dq*-frame [21]. Taking this into account, the Clarke and Park transformations cannot be applied immediately and the development is somewhat different. The main difference comes from the fact that a quadrature signal generator (QSG) is used to create an orthogonal signal to the single-phase voltages and currents measured. To create the orthogonal signal the second-order generalized integrator (SOGI)-QSG is used. The SOGI transfer function matrix is given as:

$$\mathbf{H}_{\mathrm{SOGI}}=\begin{bmatrix}\frac{K_{\mathrm{S}}\omega_s s}{s^2+K_{\mathrm{S}}\omega_s s+{\omega_s}^2} & 0\\ 0 & \frac{K_{\mathrm{S}}\omega_s s}{s^2+K_{\mathrm{S}}\omega_s s+{\omega_s}^2}\end{bmatrix}=\begin{bmatrix}H_{\mathrm{SOGI}}(s) & 0\\ 0 & H_{\mathrm{SOGI}}(s)\end{bmatrix} \tag{7}$$

As the SOGI transfer function matrix is defined as presented in Eq. (7) in $\alpha\beta$-frame, there is a need to represent it in the *dq*-frame. A similar development was already performed in [21] with the difference that the Park transformations were not defined in the same way as in this work, where the difference was in the orientation of *d* and *q* axes. Nevertheless, the final result of SOGI modelling in *dq*-frame is given as

$$\mathbf{H}_{\mathrm{SOGI}}^{\mathrm{dq}}=\begin{bmatrix}A(s) & -B(s)\\ B(s) & A(s)\end{bmatrix} \tag{8}$$

where

$$\begin{aligned}A(s)&=\frac{1}{2}\left[H_{\mathrm{SOGI}}(s+j\omega_s)+H_{\mathrm{SOGI}}(s-j\omega_s)\right]\\ B(s)&=\frac{j}{2}\left[H_{\mathrm{SOGI}}(s+j\omega_s)-H_{\mathrm{SOGI}}(s-j\omega_s)\right]\end{aligned} \tag{9}$$

More detailed derivation of the matrix Eq. (8) is given in Appendix. Apart from these remarks, the modelling process follows the same approach as the modelling of AFE. Input variables are considered to be the input voltage v_{dc} and the load current i_o. State variables are filter inductor current and capacitor voltage, i_{L} and v_{C}, which are also output variable alongside with the current on the dc-side, i_L^{dc}. The load voltage is essentially the filter capacitor voltage. The control variable is the duty cycle d^{HB}. The state-space averaged open-loop model is given in Eq. (10). The open-loop dynamics can be solved using Eq. (2) and is represented by Eq. (11).

$$\begin{bmatrix}\tilde{\mathbf{i}}_{\mathrm{L,dq}}\\ \tilde{\mathbf{v}}_{\mathrm{C,dq}}\\ \tilde{i}_L^{\mathrm{dc}}\end{bmatrix}=\begin{bmatrix}\mathbf{G}_{\mathrm{iL,o}} & \mathbf{T}_{\mathrm{oL,o}} & \mathbf{G}_{\mathrm{cL,o}}\\ \mathbf{G}_{\mathrm{iC,o}} & \mathbf{Z}_{\mathrm{out,o}} & \mathbf{G}_{\mathrm{co,o}}\\ \mathbf{Y}_{\mathrm{in,o}} & \mathbf{T}_{\mathrm{oi,o}} & \mathbf{G}_{\mathrm{ci,o}}\end{bmatrix}\begin{bmatrix}\tilde{v}_{\mathrm{dc}}\\ \tilde{\mathbf{i}}_{\mathrm{o,dq}}\\ \tilde{\mathbf{v}}_{\mathrm{C,dq}}^{\star}\end{bmatrix} \tag{11}$$

More detailed derivation of the matrix Eq. (8) is given in Appendix. Apart from these remarks, the modelling process follows the same approach as the modelling of AFE. Input

This article has been accepted for publication in a future issue of this journal, but has not been fully edited. Content may change prior to final publication. Citation information: DOI 10.1109/JESTPE.2020.2994369, IEEE Journal of Emerging and Selected Topics in Power Electronics

$$s\begin{bmatrix}\tilde{i}_{\mathrm{Ld}}\\ \tilde{i}_{\mathrm{Lq}}\\ \tilde{v}_{\mathrm{Cd}}\\ \tilde{v}_{\mathrm{Cq}}\end{bmatrix}=\underbrace{\begin{bmatrix}-\frac{R_f}{L_f} & \omega_s & -\frac{1}{L_f} & 0\\ -\omega_s & -\frac{R_f}{L_f} & 0 & -\frac{1}{L_f}\\ \frac{1}{C_f} & 0 & 0 & \omega_s\\ 0 & \frac{1}{C_f} & -\omega_s & 0\end{bmatrix}}_{\mathbf{A}}\begin{bmatrix}\tilde{i}_{\mathrm{Ld}}\\ \tilde{i}_{\mathrm{Lq}}\\ \tilde{v}_{\mathrm{Cd}}\\ \tilde{v}_{\mathrm{Cq}}\end{bmatrix}+\underbrace{\begin{bmatrix}-\frac{D_d^{\mathrm{HB}}}{L_f} & 0 & 0 & -\frac{V_{\mathrm{dc}}}{L_f} & 0\\ -\frac{D_q^{\mathrm{HB}}}{L_f} & 0 & 0 & 0 & -\frac{V_{\mathrm{dc}}}{L_f}\\ 0 & -\frac{1}{C_f} & 0 & 0 & 0\\ 0 & 0 & -\frac{1}{C_f} & 0 & 0\end{bmatrix}}_{\mathbf{B}}\begin{bmatrix}\tilde{v}_{\mathrm{dc}}\\ \tilde{i}_{\mathrm{od}}\\ \tilde{i}_{\mathrm{oq}}\\ \tilde{d}_d\\ \tilde{d}_q\end{bmatrix}$$

$$\begin{bmatrix}\tilde{i}_{\mathrm{Ld}}\\ \tilde{i}_{\mathrm{Lq}}\\ \tilde{v}_{\mathrm{Cd}}\\ \tilde{v}_{\mathrm{Cq}}\\ \tilde{i}_L^{\mathrm{dc}}\end{bmatrix}=\underbrace{\begin{bmatrix}1 & 0 & 0 & 0\\ 0 & 1 & 0 & 0\\ 0 & 0 & 1 & 0\\ 0 & 0 & 0 & 1\\ D_d^{\mathrm{HB}} & D_q^{\mathrm{HB}} & 0 & 0\end{bmatrix}}_{\mathbf{C}}\begin{bmatrix}\tilde{i}_{\mathrm{Ld}}\\ \tilde{i}_{\mathrm{Lq}}\\ \tilde{v}_{\mathrm{Cd}}\\ \tilde{v}_{\mathrm{Cq}}\end{bmatrix}+\underbrace{\begin{bmatrix}0 & 0 & 0 & 0 & 0\\ 0 & 0 & 0 & 0 & 0\\ 0 & 0 & 0 & 0 & 0\\ 0 & 0 & 0 & 0 & 0\\ 0 & 0 & 0 & I_{\mathrm{Ld}} & I_{\mathrm{Lq}}\end{bmatrix}}_{\mathbf{D}}\begin{bmatrix}\tilde{v}_{\mathrm{dc}}\\ \tilde{i}_{\mathrm{od}}\\ \tilde{i}_{\mathrm{oq}}\\ \tilde{d}_d\\ \tilde{d}_q\end{bmatrix} \tag{10}$$

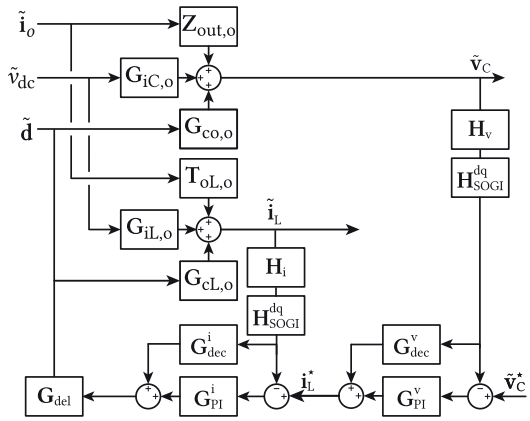

Fig. 6. Closed-loop dynamics of the HB inverter with cascaded inductor current and capacitor voltage control.

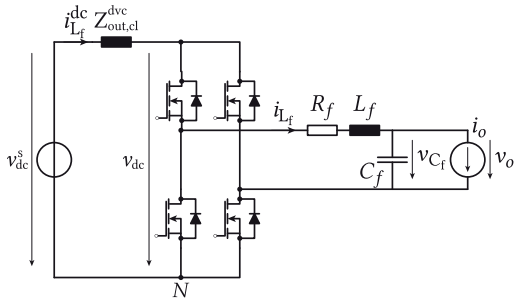

Fig. 7. HB with an output LC filter and internal source impedance that is effectively the output impedance of the AFE.

variables are considered to be the input voltage v_{dc} and the load current i_o. State variables are filter inductor current and capacitor voltage, i_{L} and v_{C}, which are also output variable alongside with the current on the dc-side, i_L^{dc}. The load voltage is essentially the filter capacitor voltage. The control variable is the duty cycle d^{HB}. The state-space averaged open-loop model is given in Eq. (10). The open-loop dynamics can be solved using Eq. (2) and is represented by Eq. (11).

$$\begin{aligned}\mathbf{G}_{\mathrm{co,cl}}^{\mathrm{lcc}}&=\mathbf{G}_{\mathrm{co,o}}\\ &\times\left[\mathbf{I}-\mathbf{G}_{\mathrm{del}}\left(\mathbf{G}_{\mathrm{PI}}^{\mathrm{i}}-\mathbf{G}_{\mathrm{dec}}^{\mathrm{i}}\right)\mathbf{H}_{\mathrm{SOGI}}^{\mathrm{dq}}\mathbf{H}_{\mathrm{i}}\mathbf{G}_{\mathrm{cL,o}}\right]^{-1}\mathbf{G}_{\mathrm{PI}}^{\mathrm{i}}\end{aligned} \tag{12}$$

In the same manner the control-to-output transfer function under the output voltage closed-loop control is given as

$$\begin{aligned}\mathbf{G}_{\mathrm{co,cl}}^{\mathrm{cvc}}&=\mathbf{G}_{\mathrm{co,cl}}^{\mathrm{lcc}}\\ &\times\left[\mathbf{I}-\left(\mathbf{G}_{\mathrm{PI}}^{\mathrm{v}}-\mathbf{G}_{\mathrm{dec}}^{\mathrm{v}}\right)\mathbf{H}_{\mathrm{SOGI}}^{\mathrm{dq}}\mathbf{H}_{\mathrm{v}}\mathbf{G}_{\mathrm{co,cl}}^{\mathrm{lcc}}\right]^{-1}\mathbf{G}_{\mathrm{PI}}^{\mathrm{v}}\end{aligned} \tag{13}$$

where $\mathbf{G}_{\mathrm{dec}}^{\mathrm{i}}$, $\mathbf{G}_{\mathrm{dec}}^{\mathrm{v}}$, $\mathbf{G}_{\mathrm{PI}}^{\mathrm{i}}$ and $\mathbf{G}_{\mathrm{PI}}^{\mathrm{v}}$ are the current and voltage controller decoupling matrices and current and voltage PI regulators respectively, while matrices $\mathbf{H}$ are current and voltage transducer matrices that take into an account the presence of SOGI and $\mathbf{G}_{\mathrm{del}}$ is the matrix that models the PWM update delay, all given in the Appendix. The closed-loop model of the single-phase inverter in *dq*-frame is given in Fig. 6 which also represents the output side dynamics. Real-time hardware-in-the-loop (HIL) simulations in the following sections will provide the model verification.

IV. Source-Affected Dynamics Characterization

In Section III-B it was stated that the dc-link voltage source is ideal with respect to the fact that the voltage was controlled on the AFE side. However, in practice the control loops do not have infinite bandwidth and as such the voltage source cannot be considered ideal. This means that the source contains a non-zero finite internal impedance which is the closed-loop output impedance $Z_{\mathrm{out,cl}}^{\mathrm{dvc}}$ of the active input element, i.e. the AFE (cf. Fig. 7). From Fig. 7 the dc-side current of the inverter can be defined as

$$i_{\mathrm{dc}}^{L}=\frac{v_{\mathrm{dc}}^{\mathrm{s}}-v_{\mathrm{dc}}}{Z_{\mathrm{out,cl}}^{\mathrm{dvc}}} \tag{14}$$

Where $v_{\mathrm{dc}}^{\mathrm{s}}$ is the dc-link voltage controlled by the AFE control system. As a reminder, closed loop dynamics of the HB is

This article has been accepted for publication in a future issue of this journal, but has not been fully edited. Content may change prior to final publication. Citation information: DOI 10.1109/JESTPE.2020.2994369, IEEE Journal of Emerging and Selected Topics in Power Electronics

given as

$$\begin{bmatrix} \tilde{\mathbf{i}}_{\mathrm{L,dq}} \\ \tilde{\mathbf{v}}_{\mathrm{C,dq}} \\ \tilde{i}_L^{\mathrm{dc}} \end{bmatrix} = \begin{bmatrix} \mathbf{G}_{\mathrm{iL,cl}}^{\mathrm{cvc}} & \mathbf{T}_{\mathrm{oL,cl}}^{\mathrm{cvc}} & \mathbf{G}_{\mathrm{cL,cl}}^{\mathrm{cvc}} \\ \mathbf{G}_{\mathrm{iC,cl}}^{\mathrm{cvc}} & \mathbf{Z}_{\mathrm{out,cl}}^{\mathrm{cvc}} & \mathbf{G}_{\mathrm{co,cl}}^{\mathrm{cvc}} \\ Y_{\mathrm{in,cl}}^{\mathrm{cvc}} & \mathbf{T}_{\mathrm{oi,cl}}^{\mathrm{cvc}} & \mathbf{G}_{\mathrm{ci,cl}}^{\mathrm{cvc}} \end{bmatrix} \begin{bmatrix} \tilde{v}_{\mathrm{dc}} \\ \tilde{\mathbf{i}}_{\mathrm{o,dq}} \\ \tilde{\mathbf{v}}_{\mathrm{C,dq}}^{\star} \end{bmatrix} \tag{15}$$

From Eq. (15) the i_{dc}^{L} can be obtained as

$$i_{\mathrm{dc}}^{L} = Y_{\mathrm{in,cl}}^{\mathrm{cvc}} v_{\mathrm{dc}} + \mathbf{G}_{\mathrm{ci,cl}}^{\mathrm{cvc}} \tilde{\mathbf{v}}_{\mathrm{C,dq}}^{\star} + \mathbf{T}_{\mathrm{oi,cl}}^{\mathrm{cvc}} \tilde{\mathbf{i}}_{\mathrm{o,dq}} \tag{16}$$

Plugging Eq. (14) into Eq. (16) gives the $v_{\mathrm{dc}}^{\mathrm{s}}$ expressed in terms of v_{dc} as

$$\tilde{v}_{\mathrm{dc}} = \frac{\tilde{v}_{\mathrm{dc}}^{\mathrm{s}} - Z_{\mathrm{out,cl}}^{\mathrm{dvc}} \mathbf{G}_{\mathrm{ci,cl}}^{\mathrm{cvc}} \tilde{\mathbf{v}}_{\mathrm{C,dq}}^{\star} - Z_{\mathrm{out,cl}}^{\mathrm{dvc}} \mathbf{T}_{\mathrm{oi,cl}}^{\mathrm{cvc}} \tilde{\mathbf{i}}_{\mathrm{o,dq}}}{1 + Z_{\mathrm{out,cl}}^{\mathrm{dvc}} Y_{\mathrm{in,cl}}^{\mathrm{cvc}}} \tag{17}$$

Replacing $\tilde{v}_{\mathrm{dc}}$ in Eq. (15) by Eq. (17) gives the model of the closed-loop source affected dynamics in Eq. (18).

V. Single-Phase Measurements in *dq*-Frame

The control-to-output characteristics $\mathbf{G}_{\mathrm{co,cl}}^{\mathrm{cvc}}$of the inverter in the *dq*-frame is a small-signal characteristic at the dc level while the actual single-phase system is an ac system and as such the characteristics cannot be directly measured in the *dq*-frame. Instead, an approach in which the measurements from a single-phase system are transferred into a *dq*-frame needs to be devised. For this purpose, a measurement and verification process based on creating two orthogonal systems is used.

A. Control-to-Output Characteristics

The $\mathbf{G}_{\mathrm{co,cl}}^{\mathrm{cvc}}$ is defined as

$$\begin{bmatrix} \tilde{v}_{\mathrm{Cd}} \\ \tilde{v}_{\mathrm{Cq}} \end{bmatrix} = \mathbf{G}_{\mathrm{co,cl}}^{\mathrm{cvc}} \begin{bmatrix} \tilde{v}_{\mathrm{Cd}}^{\star} \\ \tilde{v}_{\mathrm{Cq}}^{\star} \end{bmatrix} \tag{19}$$

To extract the frequency response of $\mathbf{G}_{\mathrm{co,cl}}^{\mathrm{cvc}}$, the process needs to be perform with two sets of voltage measurements, and thus it can be uniquely determined. $\mathbf{G}_{\mathrm{co,cl}}^{\mathrm{cvc}}$ can be calculated as

$$\mathbf{G}_{\mathrm{co,cl}}^{\mathrm{cvc}} = \begin{bmatrix} \tilde{v}_{\mathrm{Cd},1} & \tilde{v}_{\mathrm{Cd},2} \\ \tilde{v}_{\mathrm{Cq},1} & \tilde{v}_{\mathrm{Cq},2} \end{bmatrix} \begin{bmatrix} \tilde{v}_{\mathrm{Cd},1}^{\star} & \tilde{v}_{\mathrm{Cd},2}^{\star} \\ \tilde{v}_{\mathrm{Cq},1}^{\star} & \tilde{v}_{\mathrm{Cd},2}^{\star} \end{bmatrix}^{-1} \tag{20}$$

Moreover, $[\tilde{v}_{\mathrm{Cd},1}, \tilde{v}_{\mathrm{Cq},1}]$ and $[\tilde{v}_{\mathrm{Cd},2}, \tilde{v}_{\mathrm{Cq},2}]$ are linearly independent as well as $\left[\tilde{v}_{\mathrm{Cd},1}^{\star}, \tilde{v}_{\mathrm{Cq},1}^{\star}\right]$ and $\left[\tilde{v}_{\mathrm{Cd},2}^{\star}, \tilde{v}_{\mathrm{Cq},2}^{\star}\right]$. The perturbation can be injected directly in the reference voltage $\tilde{\mathbf{v}}_{\mathrm{C,dq}}^{\star}$ in the control system, but the response can only be measured on the inverter terminals in the single-phase system.

B. Wideband Perturbation Injection

Widely popular method in impedance/admittance measurements is the sine sweep, which requires one by one frequency small-signal perturbation injection and collection of response, thus requiring large number of measurements and time to be executed. If the measurement time is too long, the measured object may as well be disturbed and change its operating point and subsequently the impedance or admittance would change. This is somewhat improved with multi-tone signals but the energy of this signal is reduced with the number of tones it consists of. Recently PRBS signals (c.f. Fig. 8) have seen substantial use for system identification and impedance measurement [22]–[24]. The advantage of these signals lies in the fact that they are well suited for the characterization of dynamics systems where rapid measurement is necessary due to the possibility of variation of the system state in time. What is common for measurements in [22]–[24] is that they are performed in dc or three-phase ac systems after which the results are represented in *dq*-frame even though they represent ac measurements. Here, a method that employs the wideband PRBS signal for the control-to-output characteristics of a single-phase inverter in the *dq*-frame is presented. Measurement process of $\mathbf{G}_{\mathrm{co,cl}}^{\mathrm{cvc}}$ requires two perturbation injections and two measurement sets. First perturbation is injected into the *d*-axis voltage reference, while the *q*-axis perturbation is kept at zero value. For the second injection, the opposite holds. Thus the perturbation matrix $\mathbf{P}(t)$ in the *dq*-frame is designed as

$$\mathbf{P}(t) = \begin{bmatrix} v_{\mathrm{pd},1} & v_{\mathrm{pd},2} \\ v_{\mathrm{pq},1} & v_{\mathrm{pq},2} \end{bmatrix} = \begin{bmatrix} p(t) & 0 \\ 0 & p(t) \end{bmatrix} \tag{21}$$

where the $p(t)$ is the PRBS signal in time domain, and the perturbation is injected into the voltage reference $\tilde{\mathbf{v}}_{\mathrm{C,dq}}^{\star}$.

The idea behind the single-phase measurement of $\mathbf{G}_{\mathrm{co,cl}}^{\mathrm{cvc}}$ in *dq*-frame lies in measuring the response of two systems, one original and one orthogonal to it. For the original system, the Park transform and its inverse are given as:

$$\begin{aligned} \mathbf{T}_{\Theta} &= \begin{bmatrix} \cos\theta_s & \sin\theta_s \\ -\sin\theta_s & \cos\theta_s \end{bmatrix} \\ \mathbf{T}_{\Theta}^{-1} &= \begin{bmatrix} \cos\theta_s & -\sin\theta_s \\ \sin\theta_s & \cos\theta_s \end{bmatrix} \end{aligned} \tag{22}$$

While for the orthogonal system all the transformations and its inverse in the control algorithm are rotated by $\frac{\pi}{2}$ and are given as:

$$\begin{aligned} \overline{\mathbf{T}}_{\Theta} &= \begin{bmatrix} \cos(\theta_s - \frac{\pi}{2}) & \sin(\theta_s - \frac{\pi}{2}) \\ -\sin(\theta_s - \frac{\pi}{2}) & \cos(\theta_s - \frac{\pi}{2}) \end{bmatrix} \\ &= \begin{bmatrix} \sin\theta_s & -\cos\theta_s \\ \cos\theta_s & \sin\theta_s \end{bmatrix} \\ \overline{\mathbf{T}}_{\Theta}^{-1} &= \begin{bmatrix} \sin\theta_s & \cos\theta_s \\ -\cos\theta_s & \sin\theta_s \end{bmatrix} \end{aligned} \tag{23}$$

where $\theta_s = \omega_s t$. For this approach to be possible it is considered that one has the access to the control system, to which the authors of this work as the system designers have, since the ultimate goal is to build an MV–CHB for perturbation injection and impedance/admittance measurement. After injecting the perturbation and measuring the output voltages, the original system will provide the voltage $v_{C,\alpha}$, while the orthogonal one will provide $v_{C,\beta}$. The two voltage measurements are then combined and transformed into their *dq*-frame counterparts, thus effectively providing a way to perform single-phase measurements in *dq*-frame. Once the measurements are obtained one needs to extract the frequency

This article has been accepted for publication in a future issue of this journal, but has not been fully edited. Content may change prior to final publication. Citation information: DOI 10.1109/JESTPE.2020.2994369, IEEE Journal of Emerging and Selected Topics in Power Electronics

$$\begin{bmatrix}\tilde{\mathbf{i}}_{\mathrm{L,dq}}\\ \tilde{\mathbf{v}}_{\mathrm{C,dq}}\\ \tilde{i}_L^{\mathrm{dc}}\end{bmatrix} = \begin{bmatrix}\mathbf{G}_{\mathrm{iL,cl}}^{\mathrm{cvc}} & \mathbf{T}_{\mathrm{oL,cl}}^{\mathrm{cvc}} & \mathbf{G}_{\mathrm{cL,cl}}^{\mathrm{cvc}}\\ \mathbf{G}_{\mathrm{iC,cl}}^{\mathrm{cvc}} & \mathbf{Z}_{\mathrm{out,cl}}^{\mathrm{cvc}} & \mathbf{G}_{\mathrm{co,cl}}^{\mathrm{cvc}}\\ Y_{\mathrm{in,cl}}^{\mathrm{cvc}} & \mathbf{T}_{\mathrm{oi,cl}}^{\mathrm{cvc}} & \mathbf{G}_{\mathrm{ci,cl}}^{\mathrm{cvc}}\end{bmatrix}\begin{bmatrix}\frac{\mathbf{I}}{1+Z_{\mathrm{out,cl}}^{\mathrm{dvc}}Y_{\mathrm{in,cl}}^{\mathrm{cvc}}} & \frac{-Z_{\mathrm{out,cl}}^{\mathrm{dvc}}\mathbf{T}_{\mathrm{oi,cl}}^{\mathrm{cvc}}}{1+Z_{\mathrm{out,cl}}^{\mathrm{dvc}}Y_{\mathrm{in,cl}}^{\mathrm{cvc}}} & \frac{-Z_{\mathrm{out,cl}}^{\mathrm{dvc}}\mathbf{G}_{\mathrm{ci,cl}}^{\mathrm{cvc}}}{1+Z_{\mathrm{out,cl}}^{\mathrm{dvc}}Y_{\mathrm{in,cl}}^{\mathrm{cvc}}}\\ 0 & 0 & \mathbf{I}\\ 0 & \mathbf{I} & 0\end{bmatrix}\begin{bmatrix}\tilde{v}_{\mathrm{dc}}^{\mathrm{s}}\\ \tilde{\mathbf{i}}_{\mathrm{o,dq}}\\ \tilde{\mathbf{v}}_{\mathrm{C,dq}}^{\star}\end{bmatrix}$$

$$\begin{bmatrix}\tilde{\mathbf{i}}_{\mathrm{L,dq}}\\ \tilde{\mathbf{v}}_{\mathrm{C,dq}}\\ \tilde{i}_L^{\mathrm{dc}}\end{bmatrix} = \begin{bmatrix}\frac{\mathbf{G}_{\mathrm{iL,cl}}^{\mathrm{cvc}}}{1+Z_{\mathrm{out,cl}}^{\mathrm{dvc}}Y_{\mathrm{in,cl}}^{\mathrm{cvc}}} & \mathbf{T}_{\mathrm{oL,cl}}^{\mathrm{cvc}}-\frac{\mathbf{G}_{\mathrm{iL,cl}}^{\mathrm{cvc}}Z_{\mathrm{out,cl}}^{\mathrm{dvc}}\mathbf{T}_{\mathrm{oi,cl}}^{\mathrm{cvc}}}{1+Z_{\mathrm{out,cl}}^{\mathrm{dvc}}Y_{\mathrm{in,cl}}^{\mathrm{cvc}}} & \mathbf{G}_{\mathrm{cL,cl}}^{\mathrm{cvc}}-\frac{\mathbf{G}_{\mathrm{iL,cl}}^{\mathrm{cvc}}Z_{\mathrm{out,cl}}^{\mathrm{dvc}}\mathbf{G}_{\mathrm{ci,cl}}^{\mathrm{cvc}}}{1+Z_{\mathrm{out,cl}}^{\mathrm{dvc}}Y_{\mathrm{in,cl}}^{\mathrm{cvc}}}\\ \frac{\mathbf{G}_{\mathrm{iC,cl}}^{\mathrm{cvc}}}{1+Z_{\mathrm{out,cl}}^{\mathrm{dvc}}Y_{\mathrm{in,cl}}^{\mathrm{cvc}}} & \mathbf{Z}_{\mathrm{out,cl}}^{\mathrm{cvc}}-\frac{\mathbf{G}_{\mathrm{iL,cl}}^{\mathrm{cvc}}Z_{\mathrm{out,cl}}^{\mathrm{dvc}}\mathbf{T}_{\mathrm{oi,cl}}^{\mathrm{cvc}}}{1+Z_{\mathrm{out,cl}}^{\mathrm{dvc}}Y_{\mathrm{in,cl}}^{\mathrm{cvc}}} & \mathbf{G}_{\mathrm{co,cl}}^{\mathrm{cvc}}-\frac{\mathbf{G}_{\mathrm{iC,cl}}^{\mathrm{cvc}}Z_{\mathrm{out,cl}}^{\mathrm{dvc}}\mathbf{G}_{\mathrm{ci,cl}}^{\mathrm{cvc}}}{1+Z_{\mathrm{out,cl}}^{\mathrm{dvc}}Y_{\mathrm{in,cl}}^{\mathrm{cvc}}}\\ \frac{Y_{\mathrm{in,cl}}^{\mathrm{cvc}}}{1+Z_{\mathrm{out,cl}}^{\mathrm{dvc}}Y_{\mathrm{in,cl}}^{\mathrm{cvc}}} & \frac{\mathbf{T}_{\mathrm{oi,cl}}^{\mathrm{cvc}}}{1+Z_{\mathrm{out,cl}}^{\mathrm{dvc}}Y_{\mathrm{in,cl}}^{\mathrm{cvc}}} & \frac{\mathbf{G}_{\mathrm{ci,cl}}^{\mathrm{cvc}}}{1+Z_{\mathrm{out,cl}}^{\mathrm{dvc}}Y_{\mathrm{in,cl}}^{\mathrm{cvc}}}\end{bmatrix}\begin{bmatrix}\tilde{v}_{\mathrm{dc}}^{\mathrm{s}}\\ \tilde{\mathbf{i}}_{\mathrm{o,dq}}\\ \tilde{\mathbf{v}}_{\mathrm{C,dq}}^{\star}\end{bmatrix} \tag{18}$$

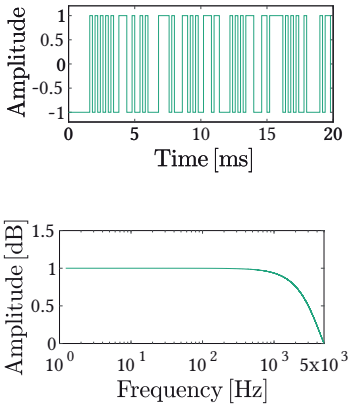

Fig. 8. PRBS-12 signal in time and frequency domain

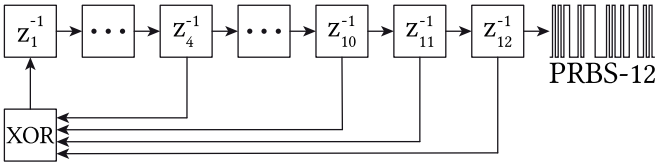

Fig. 9. Shift register circuit for PRBS generation

spectrum of the measurements and the perturbation signal using Fast Fourier Transform (FFT) algorithm upon which the equation Eq. (20) can be applied.

C. Hardware-in-the-Loop Measurement Setup

For the purposes of obtaining trustworthy results that would support mathematical modelling and offline simulations, real-time HIL system is created. The physical system is presented in Fig. 10. To main parts of the system are the RT Box real-time simulator and the TMS320F28069 MCU. Models presented in Figs. 2 and 5 are implemented in the RT Box and are used to simulate the converter structures in real-time. The grid synchronization and control of the models is deployed on the MCU as well as the perturbation signal that is injected in the output voltage reference. The signal was generated by a 12-bit-length shift register resulting in 4095-bit-long PRBS signal. The sequence was generated at $5\,\mathrm{kHz}$ generation frequency which sets the injection time at $0.819\,\mathrm{s}$. Only one sequence was injected due to the limitations in capturing the signals inside the RT Box and in order to avoid using an external

TABLE II: HB inverter parameters

$v_{\mathrm{C,d}} = 600\,\mathrm{V}$	$f_o = 50\,\mathrm{Hz}$
$v_{\mathrm{C,q}} = 0\,\mathrm{V}$	$L_f = 1.4\,\mathrm{mH}$
$i_{\mathrm{o,d}} = 60\,\mathrm{A}$	$R_f = 100\,\mathrm{m\Omega}$
$i_{\mathrm{o,q}} = 0\,\mathrm{A}$	$C_f = 24\,\mu\mathrm{H}$
$K_{\mathrm{p,lcc}} = 2.5$	$K_{\mathrm{i,lcc}} = 5$
$K_{\mathrm{p,cvc}} = 1$	$K_{\mathrm{i,cvc}} = 52$

TABLE III: MV active rectifier parameters

$P_{\mathrm{nom}} = 50 - 500\,\mathrm{kW}$	$v_{\mathrm{out}} = 10\,\mathrm{kV}$
$v_{\mathrm{in,l-l,rms}} = 5.7\,\mathrm{kV}$	$f_s = 50\,\mathrm{Hz}$
$L_{in} = 10\,\mathrm{mH}$	$R_{in} = 10\,\mathrm{m\Omega}$
$C_{\mathrm{out}} = 40\,\mathrm{mF}$	$f_{\mathrm{sw}} = 5 - 20\,\mathrm{kHz}$
$K_{\mathrm{p,cc}} = 17 - 67$	$K_{\mathrm{i,cc}} = 83 - 334$
$K_{\mathrm{p,vc}} = 6 - 22$	$K_{\mathrm{i,vc}} = 386 - 6173$

acquisition system that would require additional scaling and conversion and thus would reduce the measurement precision.

As the measurement process requires two separate systems to be implemented and perturbed there has to exist some sort of assuring that the systems are perturbed at the same operating point. This requirement is achieved by the synchronization scheme presented in Fig. 11. After the perturbation is enabled by an external signal the scheme waits until the angle of the output voltage, θ_s is zero. In this way, the original system is perturbed at the peak of the output voltage and the orthogonal at the zero voltage. Once the zero angle is detected the perturbation signal is created inside the MCU using shift-registers. Additionally, at the start and at the end of the perturbation signal two flag signals are raised which are passed to the RT Box. These flags serve as a mean of knowing which portion of the output voltage is perturbed and thus the extraction of the response to the perturbation is performed only on that part of the output voltage measurement.

VI. Results and Practical Application

To verify the ideas developed in this work, the theoretical characteristics $\mathbf{G}_{\mathrm{co,cl}}^{\mathrm{cvc}}$ of the models in equations Eqs. (10) and (18) are compared in Fig. 12. The comparison shows that in theory there is no influence of the AFE on the HB. The characteristics exhibits two resonant peaks at approximately

This article has been accepted for publication in a future issue of this journal, but has not been fully edited. Content may change prior to final publication. Citation information: DOI 10.1109/JESTPE.2020.2994369, IEEE Journal of Emerging and Selected Topics in Power Electronics

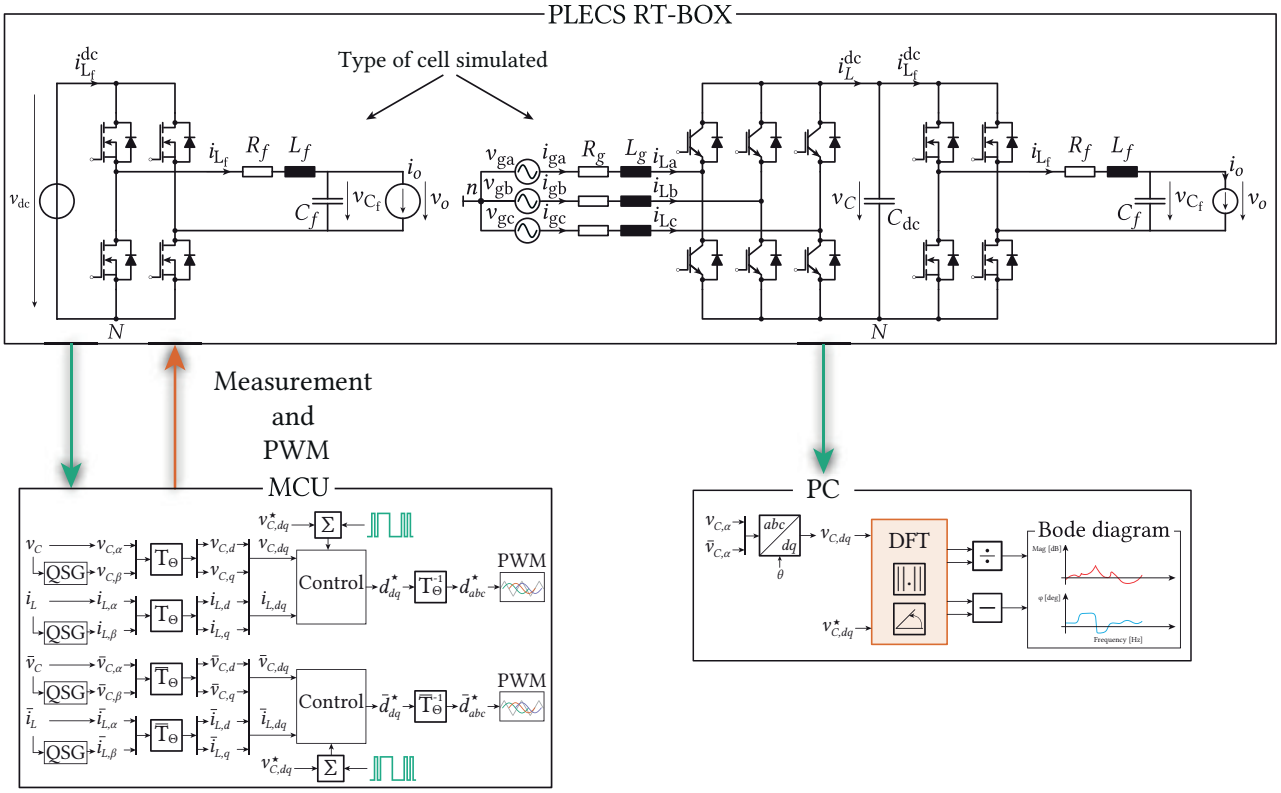

Fig. 10. Hardware-in-the-loop system, where the switching models of the converters are implemented inside the PLECS environment and are simulated in real-time on the RT-Box platform. The control for the converters is implemented on the MCU which sends the PWM signals to the RT-Box and receives the measurements from the RT-Box. Finally, the measurements from the RT-Box are extracted to a PC where the data is processed and results are obtained.

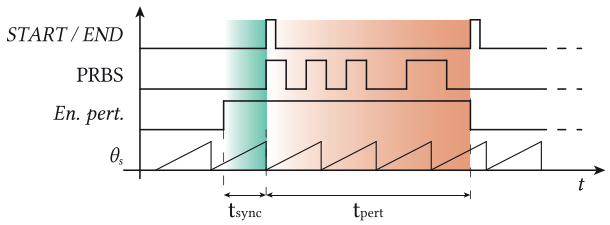

Fig. 11. Perturbation injection synchronization process. After the perturbation signal is enabled, the scheme waits for the angle to become zero after which the PRBS signal is created and injected.

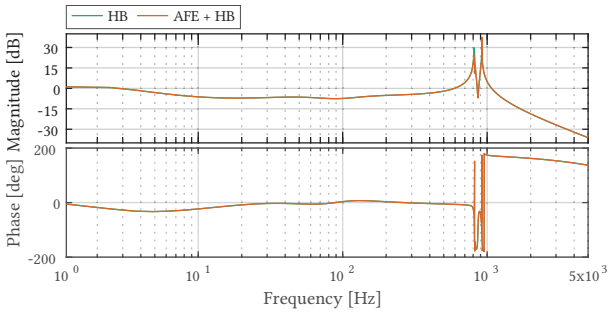

Fig. 12. Comparison of d-axis control-to-output characteristics $\mathbf{G}^{\text{cvc}}_{\text{co,cl,dd}}$ characteristics of a HB operating with an ideal dc link voltage and with AFE as an input stage controlling the dc-link voltage.

$f_{res,1} = 818\,\text{Hz}$ and $f_{res,2} = 918\,\text{Hz}$ which come from the LC-type filter resonant frequency. The resonant frequency is $f_{LC} = 868\,\text{Hz}$ in the single-phase domain but when represented in the dq-frame it is split into two points and shifted by $-f_s$ and $+f_s$, which in this particular case is $f_s = 50\,\text{Hz}$. Furthermore, the theoretical characteristics then compared against the measured one obtained using offline PLECS simulations and using HIL measurement using the setup in Fig. 10 and the procedure outlined in Section V-C. Parameters of the HB are given in Table II and they represent the steady-state voltages and currents in dq-frame, dc-link voltage, nominal output frequency output filter values and controller gains.

To examine the effect of having the AFE as an input stage two sets of results are presented in Fig. 13. Fig. 13a presents the control-to-output characteristics $\mathbf{G}^{\text{cvc}}_{\text{co,cl}}$ with an ideal voltage source at the input of the HB while the Fig. 13b represents the same characteristics with the AFE as an input. By comparing the two frequency responses it is easy to notice that there is either no or very slight difference in two characteristics. The difference in the phase angle can be attributed to the modelling of the transducer and delay transfer functions as these are an approximation of the real transfer functions. From what is presented here it can be drawn as a conclusion that the presence of an active input stage does not hinder the performance of the output one and that the two are perfectly decoupled. Practically, this means

This article has been accepted for publication in a future issue of this journal, but has not been fully edited. Content may change prior to final publication. Citation information: DOI 10.1109/JESTPE.2020.2994369, IEEE Journal of Emerging and Selected Topics in Power Electronics

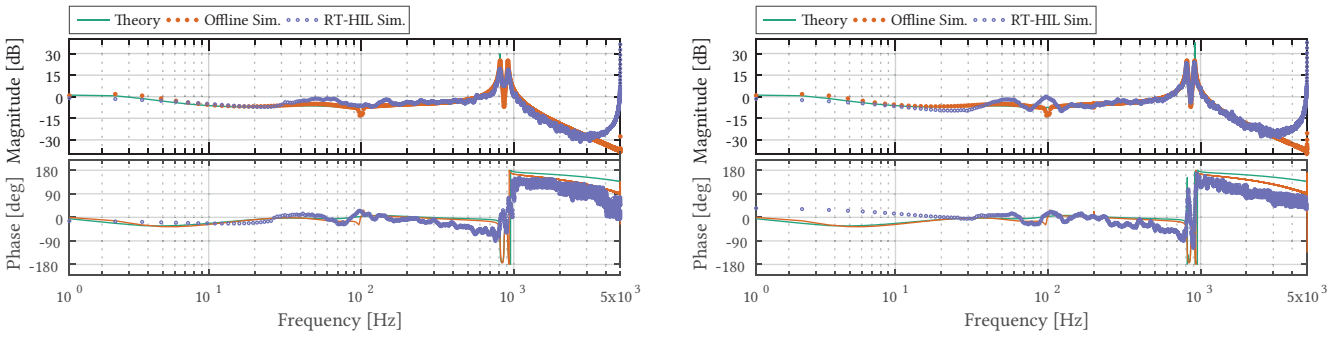

Fig. 13. **a)** d-axis control-to-output characteristics $\mathbf{G}^{\text{cvc}}_{\text{co,cl,dd}}$ with the standalone-operation of the HB-inverter compared to the same characteristics, **b)** when the AFE is operating at the input stage.

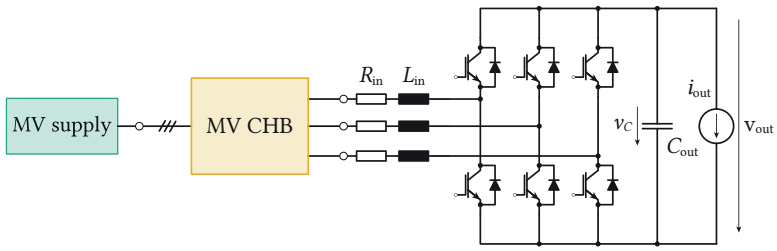

Fig. 14. Medium voltage three-phase active rectifier interfaced to a CHB (cf. Fig. 1) for small signal perturbation injection and input admittance measurement.

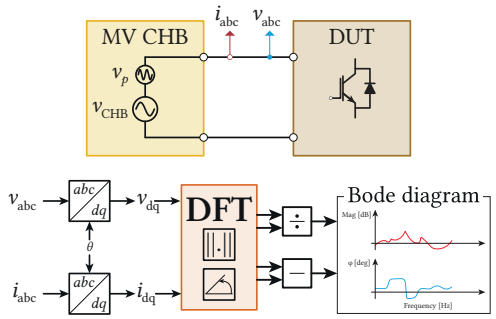

Fig. 15. Perturbation injection into an MV DUT and admittance measurement.

that all future analyses of the CHB as a topology employed for the impedance/admittance measurement can be undertaken without taking into consideration the source effects on the output stage. It should be also noted that only the d-axis control-to-output characteristics $\mathbf{G}^{\text{cvc}}_{\text{co,cl,dd}}$ is presented here. The reason for this is the fact that in reality the output of the single-phase HB inverter depends only on the characteristics in the d-axis and presenting the cross-axis characteristics would be redundant.

To demonstrate that the presented topology can be used to identify an unknown DUT, the detailed model of the CHB converter was constructed for an offline simulation and was used to inject perturbation into an MV three-phase active rectifier(cf. Fig. 14). The reasons for not performing a real-time HIL simulation in this case as well are the limited computation power and a limited number of input-output lines of the RT-Box. The voltage and current waveforms of the CHB are presented in Fig. 16. Phase-shifted PWM with $100\,\text{kHz}$ effective output frequency was used, while the line-to-line output voltage was set at $v_o = 5.7\,\text{kV}$. The perturbation injected was identical to the $5\,\text{kHz}$ PRBS presented in Fig. 8. The perturbation signal amplitude was set at $v_p = 250\,\text{V}$. In order to extract the impedance/admittance of a DUT, voltages and currents are measured at the output of the MV-CHB. These three-phase voltages are transferred into the dq-frame. A Discrete Fourier Transform (DFT) is then performed on voltages and currents in order to extract their magnitude and phase. The admittance is then extracted as

$$Y(s) = \frac{\|\tilde{i}(s)\|}{\|\tilde{v}(s)\|}\left[\angle\tilde{i}(s) - \angle\tilde{v}(s)\right] \tag{24}$$

Where $\tilde{v}(s)$ and $\tilde{i}(s)$ are the small-signal voltage perturbation and the resulting current response.

For the exact method of input admittance modelling one can refer to [18], [25]. The input and control parameters of the active rectifier are given in Table III. Two different parameters were changed to verify that the quality of identification does not depend on the change of parameters. The analytical model and the measurements from the offline simulation are given in Fig. 17, where the load was changed from $10\,\%$ load to full load. It can be noticed that the input admittance varies only in the low-frequency range. The results presented in Fig. 18 show the input admittance when the switching frequency is varied from $5\,\text{kHz}$ to $20\,\text{kHz}$. The input admittance varies in the low-frequency range with the variation of the switching frequency due to the changing control bandwidth since the increase of the switching frequency increases the control bandwidth. From the presented results it can be concluded that the CHB con-

This article has been accepted for publication in a future issue of this journal, but has not been fully edited. Content may change prior to final publication. Citation information: DOI 10.1109/JESTPE.2020.2994369, IEEE Journal of Emerging and Selected Topics in Power Electronics

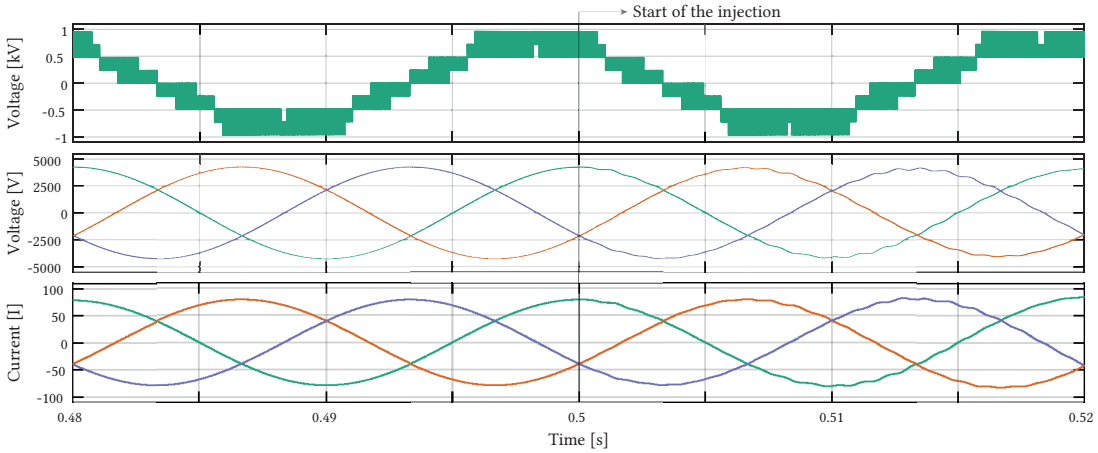

Fig. 16. (top) line-to-line voltage of the CHB measured before the output filter, (middle) output voltage of the CHB and (bottom) currents measured on the MV three-phase active rectifier side.

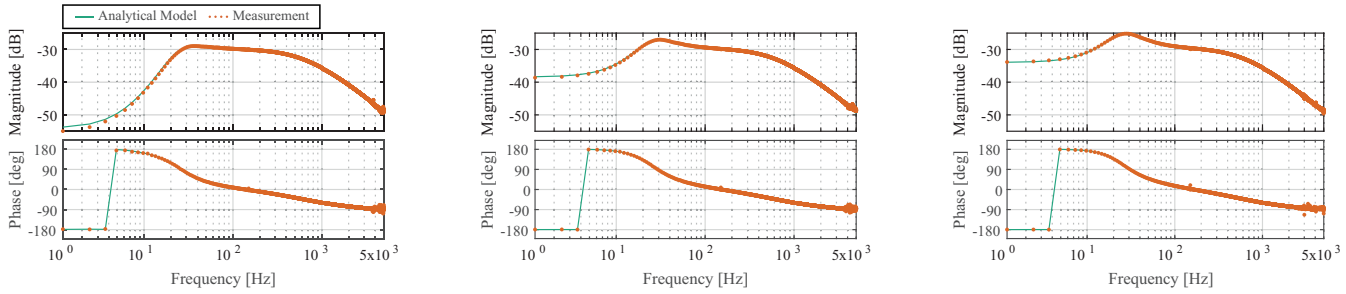

Fig. 17. d-axis input admittance $\mathbf{Y}_{\mathrm{in,dd}}$ of a 500 kW three-phase active rectifier operating at **a)** 10 %, **b)** 50 % and **c)** 100 % load. The converter is operated at $f_{\mathrm{sw}} = 10\,\mathrm{kHz}$.

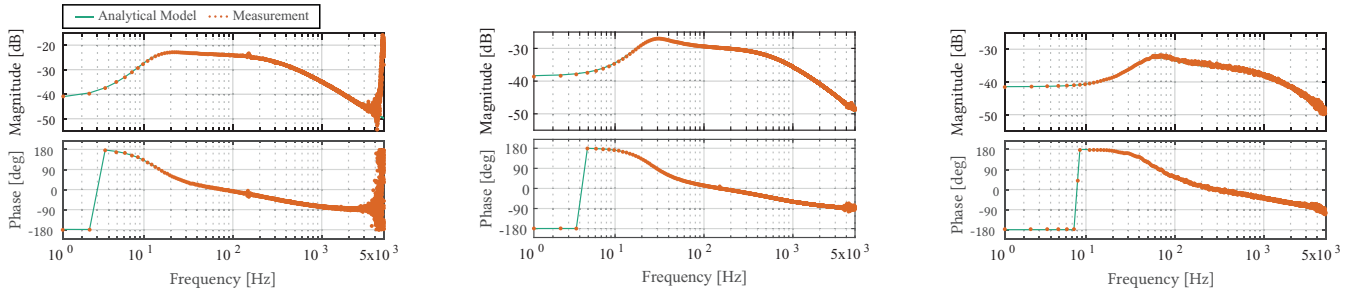

Fig. 18. d-axis input admittance $\mathbf{Y}_{\mathrm{in,dd}}$ of a 500 kW three-phase active rectifier operating at **a)** $f_{\mathrm{sw}} = 5\,\mathrm{kHz}$, **b)** $f_{\mathrm{sw}} = 10\,\mathrm{kHz}$ and **c)** $f_{\mathrm{sw}} = 20\,\mathrm{kHz}$ switching frequency.

verter can effectively be used to measure characteristics of an unknown DUT and shows itself as a promising topology than can be employed for MV impedance/admittance identification.

VII. Conclusion

This paper presented a promising solution for the problem of MV impedance/admittance measurement based on the MV-CHB converter. To confirm the suitability of the proposed idea, the model of the converter is developed systematically starting with the model of one single-phase cell of the converter and by confirming that the AFE input stage of a single cell does not affect the HB output stage dynamics. The conclusion is reached through the wideband measurement of the output dynamics using PRBS signals, while the results are shown methodically through analytical modelling, offline and real-time simulations. This type of measurement can successfully be performed in dq-frame by combining two orthogonal single-phase systems whose response is represented in the dq-frame. The real-time HIL platform measurement results add to the credibility of the results. Compared to previous measurement methods, such as the much slower ac-sweep method, the wideband measurements allow rapid verification of concepts put forward. Moreover, the use of wideband measurements, namely the use of PRBS signals, reduce the risk of the

This article has been accepted for publication in a future issue of this journal, but has not been fully edited. Content may change prior to final publication. Citation information: DOI 10.1109/JESTPE.2020.2994369, IEEE Journal of Emerging and Selected Topics in Power Electronics

measured system changing state while being measured. These, first results are vital for the development of the full scale converter as it confirms its viability in terms of the output voltage quality and control bandwidth.

Furthermore, presented simulation results show that the CHB topology can effectively be used to inject high bandwidth perturbation signals, such as the PRBS, in and unknown MV-DUT upon which the voltage and current responses can be used to obtain terminal characteristics. The perturbation injection is noninvasive and does not interfere with the steady-state operation of MV-DUT.

The proposed topology has a high potential in the domain of MV measurements due to its inherent characteristics. One is the elevated voltage output, while the other one is the high output dynamics which can be assured combining the high equivalent switching frequency and proper output control methods. Such equipment is an enabling technology for a large scale integration of MV converters and development of MVac and MVdc systems.

APPENDIX

The SOGI transfer function in the *dq*-domain is obtained by combining $\mathbf{H}_{\mathrm{SOGI}}$ and $\mathbf{T}_{\Theta}$, with the remark that the first one is an *s*-domain matrix and the second one is a time-domain matrix. For a time-domain function $x_\alpha(t)$ and its orthogonal counterpart $x_\beta(t)$, its *dq*-frame counterpart is given as:

$$\begin{aligned}\begin{bmatrix} x_d \\ x_q \end{bmatrix} &= \begin{bmatrix} \cos\theta_s & \sin\theta_s \\ -\sin\theta_s & \cos\theta_s \end{bmatrix} \begin{bmatrix} h_{\mathrm{SOGI}} * x_\alpha \\ h_{\mathrm{SOGI}} * x_\beta \end{bmatrix} \\ &= \begin{bmatrix} \cos\theta_s \left(h_{\mathrm{SOGI}} * x_\alpha\right) + \sin\theta_s \left(h_{\mathrm{SOGI}} * x_\beta\right) \\ -\sin\theta_s \left(h_{\mathrm{SOGI}} * x_\alpha\right) + \cos\theta_s \left(h_{\mathrm{SOGI}} * x_\beta\right) \end{bmatrix}\end{aligned} \tag{25}$$

where $*$ is the convolution operation. In the following developments the subscript "SOGI" is omitted to avoid clutter. Applying the property of the Laplace transform

$$\begin{aligned} h(t)\cos\theta_s &= \frac{1}{2}\left(H(s+j\omega_s) + H(s-j\omega_s)\right) \\ h(t)\sin\theta_s &= \frac{j}{2}\left(H(s+j\omega_s) - H(s-j\omega_s)\right) \end{aligned} \tag{26}$$

and replacing Eq. (26) into Eq. (25) gives Eq. (27) where the SOGI is defined in the *dq*-frame. $\mathbf{G}^{\mathrm{i}}_{\mathrm{dec}}$ and $\mathbf{G}^{\mathrm{v}}_{\mathrm{dec}}$ are the current and voltage controller decoupling matrices given as

$$\mathbf{G}^{\mathrm{i}}_{\mathrm{dec}} = \begin{bmatrix} 0 & \frac{-\omega_s L}{V_{\mathrm{dc}}} \\ \frac{\omega_s L}{V_{\mathrm{dc}}} & 0 \end{bmatrix} \tag{28}$$

$$\mathbf{G}^{\mathrm{v}}_{\mathrm{dec}} = \begin{bmatrix} 0 & -\omega_s C \\ \omega_s C & 0 \end{bmatrix} \tag{29}$$

$\mathbf{G}^{\mathrm{i}}_{\mathrm{PI}}$ and $\mathbf{G}^{\mathrm{v}}_{\mathrm{PI}}$ are the current and voltage controller matrices given as

$$\mathbf{G}^{\mathrm{i}}_{\mathrm{PI}} = \begin{bmatrix} \frac{1}{V_{\mathrm{dc}}}\left(K_{p,lcc} + \frac{K_{i,lcc}}{s}\right) & 0 \\ 0 & \frac{1}{V_{\mathrm{dc}}}\left(K_{p,lcc} + \frac{K_{i,lcc}}{s}\right) \end{bmatrix} \tag{30}$$

$$\mathbf{G}^{\mathrm{v}}_{\mathrm{PI}} = \begin{bmatrix} \left(K_{p,cvc} + \frac{K_{i,cvc}}{s}\right) & 0 \\ 0 & \left(K_{p,cvc} + \frac{K_{i,cvc}}{s}\right) \end{bmatrix} \tag{31}$$

$\mathbf{H}_{\mathrm{i}}$ and $\mathbf{H}_{\mathrm{v}}$ are the current and voltage transducer matrices and they represent the analog-to-digital conversion and sampling delay between the RT-Box and the MCU. $\mathbf{G}_{\mathrm{del}}$ represents a pure delay of half of a sampling period due to the PWM update action. The matrices are given as:

$$\mathbf{H} = \begin{bmatrix} \frac{1-\frac{T_{\mathrm{sw}}}{2}s}{1+\frac{T_{\mathrm{sw}}}{2}s} & 0 \\ 0 & \frac{1-\frac{T_{\mathrm{sw}}}{2}s}{1+\frac{T_{\mathrm{sw}}}{2}s} \end{bmatrix} \tag{32}$$

$$\mathbf{G}_{\mathrm{del}} = \begin{bmatrix} \frac{1-\frac{T_{\mathrm{sw}}}{4}s}{1+\frac{T_{\mathrm{sw}}}{4}s} & 0 \\ 0 & \frac{1-\frac{T_{\mathrm{sw}}}{4}s}{1+\frac{T_{\mathrm{sw}}}{4}s} \end{bmatrix} \tag{33}$$

REFERENCES

[1] X. Wang and F. Blaabjerg, "Harmonic Stability in Power Electronic Based Power Systems: Concept, Modeling, and Analysis," *IEEE Transactions on Smart Grid*, pp. 1–1, 2018.

[2] U. Javaid, F. D. Freijedo, D. Dujic, and W. Van Der Merwe, "Dynamic Assessment of Source–Load Interactions in Marine MVDC Distribution," *IEEE Transactions on Industrial Electronics*, vol. 64, no. 6, pp. 4372–4381, 2017.

[3] A. Riccobono and E. Santi, "Comprehensive Review of Stability Criteria for DC Power Distribution Systems," *IEEE Transactions on Industry Applications*, vol. 50, no. 5, pp. 3525–3535, Sep. 2014.

[4] Y. A. Familiant, J. Huang, K. A. Corzine, and M. Belkhayat, "New techniques for measuring impedance characteristics of three-phase AC power systems," *IEEE Transactions on Power Electronics*, vol. 24, no. 7, pp. 1802–1810, 2009.

[5] T. Roinila, M. Vilkko, and J. Sun, "Broadband methods for online grid impedance measurement," in *2013 IEEE Energy Conversion Congress and Exposition*, Sep. 2013, pp. 3003–3010.

[6] D. Martin, E. Santi, and A. Barkley, "Wide bandwidth system identification of AC system impedances by applying perturbations to an existing converter," in *2011 IEEE Energy Conversion Congress and Exposition*, Sep. 2011, pp. 2549–2556.

[7] M. Jakšić, Z. Shen, I. Cvetković, D. Boroyevich, R. Burgos, C. DiMarino, and F. Chen, "Medium-Voltage Impedance Measurement Unit for Assessing the System Stability of Electric Ships," *IEEE Transactions on Energy Conversion*, vol. 32, no. 2, pp. 829–841, Jun. 2017.

[8] F. Hahn, S. Brüske, B. Benkendorff, G. Büticchi, F. W. Füchs, and M. Liserre, "Wide frequency range medium-voltage grid impedance analysis by current injection of a multi-MW power converter," in *2016 18th European Conference on Power Electronics and Applications (EPE'16 ECCE Europe)*, Sep. 2016, pp. 1–10.

This article has been accepted for publication in a future issue of this journal, but has not been fully edited. Content may change prior to final publication. Citation information: DOI 10.1109/JESTPE.2020.2994369, IEEE Journal of Emerging and Selected Topics in Power Electronics

$$\begin{aligned}\begin{bmatrix}X_d(s)\\X_q(s)\end{bmatrix} &= \begin{bmatrix}\frac{1}{2}\left(H(s+j\omega_s)X_\alpha(s+j\omega_s)+H(s-j\omega_s)X_\alpha(s-j\omega_s)\right)\\-\frac{j}{2}\left(H(s+j\omega_s)X_\alpha(s+j\omega_s)-H(s-j\omega_s)X_\alpha(s-j\omega_s)\right)\\ \quad+\frac{j}{2}\left(H(s+j\omega_s)X_\beta(s+j\omega_s)-H(s-j\omega_s)X_\beta(s-j\omega_s)\right)\\ \quad+\frac{1}{2}\left(H(s+j\omega_s)X_\beta(s+j\omega_s)+H(s-j\omega_s)X_\beta(s-j\omega_s)\right)\end{bmatrix}\\ &= \underbrace{\begin{bmatrix}A(s) & -B(s)\\B(s) & A(s)\end{bmatrix}}_{\mathbf{H}_{\mathrm{SOGI}}^{\mathrm{dq}}(s)}\begin{bmatrix}\frac{1}{2}\left(X_\alpha(s+j\omega_s)+X_\alpha(s-j\omega_s)\right)+\frac{j}{2}\left(X_\beta(s+j\omega_s)-X_\beta(s-j\omega_s)\right)\\\frac{j}{2}\left(X_\alpha(s+j\omega_s)-X_\alpha(s-j\omega_s)\right)+\frac{1}{2}\left(X_\beta(s+j\omega_s)+X_\beta(s-j\omega_s)\right)\end{bmatrix}\\ &\text{where}\qquad A(s)=\frac{1}{2}\left[H(s+j\omega_s)+H(s-j\omega_s)\right]\qquad B(s)=\frac{j}{2}\left[H(s+j\omega_s)-H(s-j\omega_s)\right]\end{aligned} \tag{27}$$

[9] E. Ledezma, Kaiyu Wang, T. Keister, R. Edwards, R. Pipho, B. Palle, D. Kulkarni, T. E. Salem, J. C. Fox, and L. Parsa, "Development of a modular configurable multi-megawatt power amplifier," in *IECON 2013 - 39th Annual Conference of the IEEE Industrial Electronics Society*, Nov. 2013, pp. 631–636.

[10] F. Bogdan, J. Hauer, J. Langston, K. Schoder, M. Steurer, I. Cvetkovic, Z. Shen, M. Jaksic, C. DiMarino, F. Chen, D. Boroyevich, and R. Burgos, "Test environment for a novel medium voltage impedance measurement unit," in *2015 IEEE Electric Ship Technologies Symposium (ESTS)*, Jun. 2015, pp. 99–103.

[11] U. Javaid, F. D. Freijedo, W. van der Merwe, and D. Dujic, "Stability Analysis of Multi-Port MVDC Distribution Networks for All-Electric Ships," *IEEE Journal of Emerging and Selected Topics in Power Electronics*, pp. 1–1, 2019.

[12] M. Mogorovic and D. Dujic, "100 kW, 10 kHz Medium-Frequency Transformer Design Optimization and Experimental Verification," *IEEE Transactions on Power Electronics*, vol. 34, no. 2, pp. 1696–1708, Feb. 2019.

[13] M. Utvic, S. Milovanovic, and D. Dujic, "Flexible Medium Voltage DC Source Utilizing Series Connected Modular Multilevel Converters," in *2019 21st European Conference on Power Electronics and Applications (EPE'19 ECCE Europe)*, 2019.

[14] M. Petković, N. Hildebrandt, F. D. Freijedo, and D. Dujić, "Cascaded H-Bridge Multilevel Converter for a High-Power Medium-Voltage Impedance-Admittance Measurement Unit," in *2018 International Symposium on Industrial Electronics (INDEL)*, Nov. 2018, pp. 1–8.

[15] Y. Li, Y. Wang, R. Wang, J. Wu, H. Zhang, Y. Feng, S. Li, W. Yao, and B. Q. Li, "Distributed Generation Grid-Connected Converter Testing Device Based on Cascaded H-Bridge Topology," *IEEE Transactions on Industrial Electronics*, vol. 63, no. 4, pp. 2143–2154, Apr. 2016.

[16] N. Hildebrandt and D. Dujic, "Supply Grid Synchronization and Operation of a Filterless Cascaded H-Bridge based Grid Emulator," in *The 45th Annual Conference of the IEEE Industrial Electronics Society-IECON 2019*, 2019.

[17] R. W. Erickson and D. Maksimovic, *Fundamentals of power electronics*. Springer Science & Business Media, 2007.

[18] T. Suntio, T. Messo, and J. Puukko, *Power Electronic Converters: Dynamics and Control in Conventional and Renewable Energy Applications*. Wiley, 2017.

[19] V. Blasko and V. Kaura, "A new mathematical model and control of a three-phase AC-DC voltage source converter," *IEEE Transactions on Power Electronics*, vol. 12, no. 1, pp. 116–123, Jan. 1997.

[20] Y. Dai, H. Wang, and G. Zeng, "Double closed-loop pi control of three-phase inverters by binary-coded extremal optimization," *IEEE Access*, vol. 4, pp. 7621–7632, 2016.

[21] Y. Liao, Z. Liu, H. Zhang, and B. Wen, "Low-Frequency Stability Analysis of Single-Phase System With dq-Frame Impedance Approach—Part I: Impedance Modeling and Verification," *IEEE Transactions on Industry Applications*, vol. 54, no. 5, pp. 4999–5011, Sep. 2018.

[22] R. Luhtala, T. Roinila, and T. Messo, "Implementation of Real-Time Impedance-Based Stability Assessment of Grid-Connected Systems Using MIMO-Identification Techniques," *IEEE Transactions on Industry Applications*, vol. 54, no. 5, pp. 5054–5063, Sep. 2018.

[23] T. Roinila, H. Abdollahi, S. Arrua, and E. Santi, "Real-Time Stability Analysis and Control of Multiconverter Systems by Using MIMO-Identification Techniques," *IEEE Transactions on Power Electronics*, vol. 34, no. 4, pp. 3948–3957, Apr. 2019.

[24] T. Roinila, T. Messo, R. Luhtala, R. Scharrenberg, E. C. W. de Jong, A. Fabian, and Y. Sun, "Hardware-in-the-Loop Methods for Real-Time Frequency-Response Measurements of on-Board Power Distribution Systems," *IEEE Transactions on Industrial Electronics*, vol. 66, no. 7, pp. 5769–5777, Jul. 2019.

[25] L. Harnefors, M. Bongiorno, and S. Lundberg, "Input-Admittance Calculation and Shaping for Controlled Voltage-Source Converters," *IEEE Transactions on Industrial Electronics*, vol. 54, no. 6, pp. 3323–3334, Dec. 2007.

This article has been accepted for publication in a future issue of this journal, but has not been fully edited. Content may change prior to final publication. Citation information: DOI 10.1109/JESTPE.2020.2994369, IEEE Journal of Emerging and Selected Topics in Power Electronics

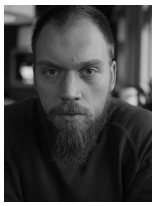

Marko Petković Marko Petković (M'16) received the B.S. degree in electrical engineering and M.S. degree in smart grid science and technology at École Polytechnique Fédérale de Lausanne (EPFL), Lausanne, Switzerland, in 2014 and 2016, respectively. Since August 2017, he is a Doctoral Assistant with the Power Electronics Laboratory at École Polytechnique Fédérale de Lausanne (EPFL), Lausanne, Switzerland. His research is focused on medium-voltage impedance / admittance measurement and system identification.

Drazen Dujic Drazen Dujic (S'03-M'09-SM'12) received the Dipl.-Ing. and M.Sc. degrees from the University of Novi Sad, Novi Sad, Serbia, in 2002 and 2005, respectively, and the Ph.D. degree from the Liverpool John Moores University, Liverpool, U.K., in 2008, all in electrical engineering. From 2002 to 2006, he was with the Department of Electrical Engineering, University of Novi Sad as a Research Assistant, and from 2006 to 2009 with Liverpool John Moores University as a Research Associate. From 2009 till 2013, he was with ABB Corporate Research Centre, Switzerland, as a Principal Scientist working on the power electronics projects spanning the range from low-voltage/power SMPS in below kilowatt range to medium voltage high-power converters in a megawatt range. From 2013 till 2014, he was with ABB Medium Voltage Drives, Turgi, Switzerland, as R&D Platform Manager, responsible for ABB's largest IGCT based medium voltage drive - ACS6000. He is currently with École Polytechnique Fédérale de Lausanne (EPFL), Lausanne, Switzerland, as an Assistant Professor and the Director of the Power Electronics Laboratory. His current research interests include the areas of design and control of advanced high-power electronics systems and high performance drives. He has authored or coauthored more than 150 scientific publications and has filed 14 patents. He is an Associate Editor for IEEE Transactions on Industrial Electronics, IEEE Transaction on Power Electronics and IET Electric Power Applications. In 2018 he has received EPE Outstanding Service Award from European Power Electronics and Drives Association, and in 2014 the Isao Takahashi Power Electronics Award for outstanding achievement in power electronics.